Available online at www.sciencedirect.com
SCIENCE DIRECT®
Journal of the Mechanics and Physics of solids
53 (2005) 1650–1685
JOURNAL OF THE MECHANICS AND PHYSICS OF SOLIDS
www.elsevier.com/locate/jmps

Multiscale modeling of the dynamics of solids at finite temperature

Xiantao Li[a,*], Weinan E[b]

[a]*Program in Applied and Computational Mathematics, Princeton University, Princeton, NJ 08544, USA*
[b]*Department of Mathematics and Program in Applied and Computational Mathematics, Princeton University, Princeton, NJ 08544, USA*

Received 30 June 2004; received in revised form 27 January 2005; accepted 31 January 2005

Abstract

We develop a general multiscale method for coupling atomistic and continuum simulations using the framework of the heterogeneous multiscale method (HMM). Both the atomistic and the continuum models are formulated in the form of conservation laws of mass, momentum and energy. A macroscale solver, here the finite volume scheme, is used everywhere on a macrogrid; whenever necessary the macroscale fluxes are computed using the microscale model, which is in turn constrained by the local macrostate of the system, e.g. the deformation gradient tensor, the mean velocity and the local temperature. We discuss how these constraints can be imposed in the form of boundary conditions. When isolated defects are present, we develop an additional strategy for defect tracking. This method naturally decouples the atomistic time scales from the continuum time scale. Applications to shock propagation, thermal expansion, phase boundary and twin boundary dynamics are presented.

Keywords: Multiscale modeling; Phase transformation

*Corresponding author. Tel.: +1 6092583685; fax: +1 6092581735.
E-mail address: xli@math.princeton.edu (X. Li).

0022-5096/$ - see front matter © 2005 Elsevier Ltd. All rights reserved.
doi:10.1016/j.jmps.2005.01.008

1. Introduction

Multiscale modeling methods that couple atomistic simulations with continuum description have attracted a great deal of attention in recent years and have shown a great deal of promise (Lu and Kaxiras, 2005). As is discussed in E and Li (2005) and E et al. (2004), most existing methods are based on coarse graining the energy, the most successful example so far being the quasicontinuum method (Tadmor et al., 1996). A coarse-grained Hamiltonian is formed, either through using representative atoms as in the quasicontinuum method (Tadmor et al., 1996), or through dividing the computational domain into atomistic and continuum regions as in Abraham et al. (1998). The coarse-grained Hamiltonian is then minimized to find the equilibrium state, or used in Hamilton's equation to model the dynamics of the system (Rudd and Broughton, 1998; Abraham et al., 1998). These methods have been very demonstrated in a number of applications. The quasicontinuum method, in particular, has been very successful in studying the structure of isolated defects at zero temperature (Tadmor et al., 1996).

Another popular idea that has been pursued is based on the domain decomposition strategy, as in Abraham et al. (1998) and Wagner and Liu (2003). The computational domain is decomposed in two atomistic and continuum regions on which the atomistic and continuum models are used, respectively, and some matching condition is devised for the continuum-atomistic interface (Cai et al., 2000; E and Huang, 2001, 2002; Wagner et al., 2004).

There seem to be some intrinsic difficulties in extending these methodologies to study dynamics and finite temperature systems. One most obvious obstacle is the issue of time scales. Even though the domain decomposition approach addresses the spatial scale issue, time scales are stilled coupled between the atomistic and continuum regions. Energy-based methods have the additional difficulty that free energy at finite temperature is not readily accessible by atomistic simulations.

The main purpose of the present paper is to provide an alternative multiscale strategy which is based directly on dynamics, i.e. the universal conservations laws that are satisfied both at the macroscopic and the microscopic levels. We demonstrate through a number of examples some features of this new strategy, including the decoupling of time scales, the ability to deal with thermal effects and of course, the ability to model dynamics.

To put things into perspective, let us discuss in more detail some of the existing multiscale methods for solids. We begin with the quasicontinuum method (Shenoy et al., 1998, 1999; Tadmor et al., 1996; Knap and Ortiz, 2001) (see also Brandt, 2002) which can be viewed as a way of simulating the nonlinear deformation of crystalline solids, but using directly models of molecular mechanics instead of continuum nonlinear elasticity. The basic setup is a finite element method on an adaptively generated mesh that reflects the local deformation of the material. Near defects such as cracks or dislocations, the mesh is refined to the atomic scale and the local energy is computed by summing directly the contribution from each atom nearby. Away

from defects, the mesh is coarsened to resolve the deformation of the material on a macroscale, and the contribution to the energy is computed by either using the Cauchy–Born rule or by summing over small clusters of atoms around a set of representative atoms (Knap and Ortiz, 2001). Quasicontinuum method has proven to be a very powerful tool for studying the quasistatic structures of solids at zero temperature (Miller and Tadmor, 2002).

Also notable was the work of Abraham et al. (1998) and Broughton et al. (1999) (called MAAD), which couples together three different models: the tight-binding quantum mechanical model, molecular dynamics and continuum elasticity. The main step is to construct a Hamiltonian that represents the total energy of the entire system which can then be used to generate time evolution. This Hamiltonian has a total of five terms, one for each of the tight-binding, molecular dynamics and continuum mechanics region, and two for the tight-binding/molecular dynamics and molecular dynamics/continuum interfaces. The method has been applied to the simulation of crack propagation in silicon.

Coarse-Grained Molecular Dynamics (CGMD) (Rudd and Broughton, 1998) is another coarse-graining procedure based on the Hamiltonian formulation. In CGMD a coarse-grained Hamiltonian is obtained by integrating out from the canonical ensemble the excess degrees of freedom.

Another issue that has attracted some attention is the matching conditions at the atomistic–continuum interface. Ideally we would like to impose the so-called transparent boundary condition so that the presence of the boundary does not influence the results in the atomistic region as if the microscale simulation is done in the whole space. In principle for linear problems at least, one can find exact boundary conditions that fulfill this task, as was discussed by Cai et al. (2000). Further work along this line was done in Wagner et al. (2004). In practice, however, it is usually too expensive to find such boundary conditions since they tend to be nonlocal and memory-dependent. This is especially true when the atomistic regions change in time, e.g. in order to track a moving defect. A practical solution was found in the work of E and Huang (2001, 2002) in which a simplified set of boundary conditions were developed that maximize the accuracy at the large scale and minimize the total reflection of phonons at the small scale. These boundary conditions have been used in a coupled atomistic–continuum scheme and applied successfully to dynamic (in contrast to quasistatic) simulations of fracture, friction between crystalline surfaces and models of dislocation dynamics (E and Huang, 2002). However the work in E and Huang (2002) was restricted to the coupling of linear elasticity with molecular dynamics at zero temperature.

Other methodologies include the scale decomposition method by Wagner and Liu (2003), the exponential Cauchy–Born rule for modeling nanotubes (Arroyo and Belytschko, 2000) and the local Cauchy–Born rule for modeling curved objects such as membranes, rods and plates (Yang, 2006).

The main task for this paper is to present a general strategy for coupled atomistic–continuum simulation of the dynamics of crystalline solids at finite temperature. This is done using the framework of heterogeneous multiscale method

(HMM for short) (E and Engquist, 2002). HMM is a general strategy for multiscale modeling. The philosophy of HMM is to start with a macroscale solver and find the missing macroscale data such as the constitutive laws and kinetic relation by performing local simulations of the microscale models constrained to be consistent with the local macroscale state of the system. HMM has been applied to a wide variety of problems, including homogenization, complex fluids, multiscale ODEs and interface problems, etc. It offers a general methodology for multiscale modeling, and it has a number of unique features compared with some other related methods. For more details see a recent review (E et al., submitted).

To discuss how the HMM philosophy can be applied to the modeling of solids, we first distinguish two different classes of multiscale problems. The first class, called type A problems, are problems with isolated defects, such as cracks, dislocations and phase boundaries. In these problems, coupling with microscale models is needed near the defects in order to accurately model properties of the defects. The second class, called type B problems, are problems for which constitutive relations are missing, and have to be obtained from the microscale models.

For both types of problems, our fundamental macroscopic model is the conservation laws of mass, momentum and energy. Therefore the first step in coupling with molecular dynamics is to express molecular dynamics in the same form. Since the macroscale model is a system of conservation laws, we choose as the macroscale solver popular methods that have been developed for solving conservation laws. In this paper we will work with finite volume methods. But other methods, such as discontinuous Galerkin method can also be used.

When implementing the selected macroscale solver, we immediately face the problem that not all the data that we need are available to us. These missing data could be the constitutive relations for type B problems, or the structural information for the defects for type A problems. We therefore estimate these data by performing local MD simulations. The MD simulations are constrained so that they are consistent with the local macrostate of the system. A very crucial component of our method is how to enforce such constraints. These will be discussed in later sections.

For type A problems we need to deal separately with the defects. In this case we distinguish two different cases according to whether there is scale separation between the time scale for the dynamics of the defect, T_d, and the time scale for the relaxation of the defect structure, T_r. If T_d is much larger than T_r, we can effectively treat the problem as a type B problem, by extending the macroscale model to include the dynamics and the local environment of the defects. The resulting algorithm is a multiscale defect tracking procedure. If T_d is comparable with T_r, we model the whole time history of the defects using the atomistic model. In this case, our methodology resembles that of adaptive model refinement (see Fig. 8).

Next we first describe the macroscopic and microscopic models that will be used in our method. The rest of the paper is then divided into two parts: type B problems in Section 3, where we deal with constitutive deficiency, and type A problems in Section 4 where we consider isolated defects.

2. Macroscopic and microscopic models

In atomistic models such as molecular dynamics (MD), the system is described by the position and momentum of each individual atom in the system. The dynamics of the atoms obey Newton's law:

$$\begin{aligned} &\dot{\mathbf{x}}_i = \mathbf{v}_i, \\ &m_i \dot{\mathbf{v}}_i = -\nabla_{\mathbf{x}_i} V, \end{aligned} \tag{1}$$

where m_i denotes the mass of the ith atom, and $V(\mathbf{x}_1, \mathbf{x}_2, \ldots, \mathbf{x}_N)$ is the interatomic potential. For simplicity we will first focus on the case of pairwise interaction potential, ϕ, even though pairwise potentials are usually inadequate for modeling solids. Extension to general potentials are discussed in the appendix. We emphasize that neither the numerical method nor the numerical results is limited to pair potentials.

The continuum models are usually expressed as a set of partial differential equations (PDEs) in the form of conservation laws. For instance in Eulerian coordinates, we can write the conservation of mass (ρ), momentum ($\mathbf{q}$) and energy (E) in the following form:

$$\begin{aligned} &\partial_t \rho + \nabla_{\mathbf{x}} \cdot \mathbf{q} = 0, \\ &\partial_t \mathbf{q} - \nabla_{\mathbf{x}} \cdot \boldsymbol{\tau} = 0, \\ &\partial_t E + \nabla_{\mathbf{x}} \cdot \mathbf{J} = 0. \end{aligned} \tag{2}$$

Here ∂_t indicates the time derivative in a fixed coordinate, $\boldsymbol{\tau}$ is the stress tensor and $\mathbf{J}$ is the energy flux.

For solids it is more convenient to work with Lagrangian coordinates. Denote by $\mathbf{x}^0$ the reference coordinate of the solid and $\mathbf{x} = \mathbf{x}^0 + \mathbf{u}(\mathbf{x}^0, t)$, the position after deformation, with $\mathbf{u}$ being the displacement. Then the conservation laws take the form:

$$\begin{aligned} &\partial_t \mathbf{A} - \nabla_{\mathbf{x}^0} \mathbf{v} = 0, \\ &\partial_t \mathbf{q} - \nabla_{\mathbf{x}^0} \cdot \boldsymbol{\sigma} = 0, \\ &\rho_0 \partial_t e + \nabla_{\mathbf{x}^0} \cdot \mathbf{j} = 0. \end{aligned} \tag{3}$$

Here $\mathbf{A}, \mathbf{v}, e$ are the deformation gradient, velocity and total energy per particle respectively, ρ_0 is the initial density, $\boldsymbol{\sigma}$ is the first Piola–Kirchhoff stress tensor and $\mathbf{j}$ is the energy flux. The first equation in Eq. (3) describes the time evolution of the deformation; the second and third equations are conservation of momentum and energy, respectively. In continuum mechanics, for instance Landau (1986), these equations are supplemented by the empirical constitutive relations for stress and energy fluxes. Our concern in the present paper is to develop multiscale strategies that bypass these empirical constitutive laws when their accuracy is in doubt.

Our basic starting point for coupling MD with the continuum model is to express MD in the form of Eqs. (2) and (3). For this purpose, we define the following

empirical distributions (Irving and Kirkwood, 1950):

$$\widetilde{\rho}(\mathbf{x},t)=\sum_i m_i\delta(\mathbf{x}-\mathbf{x}_i(t)), \tag{4a}$$

$$\widetilde{\mathbf{q}}(\mathbf{x},t)=\sum_i m_i\mathbf{v}_i(t)\delta(\mathbf{x}-\mathbf{x}_i(t)), \tag{4b}$$

$$\widetilde{E}(\mathbf{x},t)=\sum_i\left[\frac{1}{2}m_i\mathbf{v}_i^2+\frac{1}{2}\sum_{j\neq i}\phi(\mathbf{x}_i(t)-\mathbf{x}_j(t))\right]\delta(\mathbf{x}-\mathbf{x}_i(t)), \tag{4c}$$

where $\delta(\cdot)$ is the delta function. From Eq. (1), we have

$$\begin{aligned}&\partial_t\widetilde{\rho}+\nabla_{\mathbf{x}}\cdot\widetilde{\mathbf{q}}=0,\\&\partial_t\widetilde{\mathbf{q}}-\nabla_{\mathbf{x}}\cdot\widetilde{\boldsymbol{\tau}}=0,\\&\partial_t\widetilde{E}+\nabla_{\mathbf{x}}\cdot\widetilde{\mathbf{J}}=0,\end{aligned} \tag{5}$$

where the fluxes are given by

$$\begin{aligned}\widetilde{\tau}_{\alpha\beta}(\mathbf{x},t)=&-\sum_i m_i v_{i\alpha}v_{i\beta}\delta(\mathbf{x}-\mathbf{x}_i(t))\\&-\frac{1}{2}\sum_i\sum_{j\neq i}f_\alpha(\mathbf{x}_i-\mathbf{x}_j)(x_{i\beta}-x_{j\beta})\\&\times\int_0^1\delta(\mathbf{x}-(\mathbf{x}_j+\lambda(\mathbf{x}_i-\mathbf{x}_j)))\,\mathrm{d}\lambda,\end{aligned} \tag{6a}$$

$$\begin{aligned}\widetilde{\mathbf{J}}(\mathbf{x},t)=&\sum_i\mathbf{v}_i\left[m_i\frac{1}{2}\mathbf{v}_i^2+\frac{1}{2}\sum_{j\neq i}\phi(\mathbf{x}_i-\mathbf{x}_j)\right]\delta(\mathbf{x}-\mathbf{x}_i(t))\\&+\frac{1}{4}\sum_{j\neq i}(\mathbf{v}_j+\mathbf{v}_i)\cdot\mathbf{f}(\mathbf{x}_j-\mathbf{x}_i)(\mathbf{x}_i-\mathbf{x}_j)\\&\times\int_0^1\delta(\mathbf{x}-(\mathbf{x}_j+\lambda(\mathbf{x}_i-\mathbf{x}_j)))\,\mathrm{d}\lambda.\end{aligned} \tag{6b}$$

Here $\mathbf{f}(\mathbf{x}_i-\mathbf{x}_j)=(f_1,f_2,f_3)(\mathbf{x}_i-\mathbf{x}_j)$ is the force between the ith and jth particles. To derive Eq. (6), the following fact is useful:

$$\nabla_{\mathbf{x}}\cdot\left[(\mathbf{x}_i-\mathbf{x}_j)\int_0^1\delta(\mathbf{x}-(\mathbf{x}_j+\lambda(\mathbf{x}_i-\mathbf{x}_j)))\,\mathrm{d}\lambda\right]=\delta(\mathbf{x}-\mathbf{x}_j)-\delta(\mathbf{x}-\mathbf{x}_i).$$

One can compute the spatial average of the stress defined in Eq. (6) over some domain Ω, which yields

$$-\frac{1}{|\Omega|}\left(\sum_{\mathbf{x}_i\in\Omega}m_i\mathbf{v}_i\otimes\mathbf{v}_i+\frac{1}{2}\sum_i\sum_{j\neq i}\mathbf{f}(\mathbf{x}_i-\mathbf{x}_j)\otimes(\mathbf{x}_i-\mathbf{x}_j)c_{ij}\right)$$

with c_{ij} being the fraction of the ij bond that lies inside of the domain (for periodic system, $c_{ij} \equiv 1$). This is immediately recognized to be the virial stress. The momentum equation in Eq. (5) indicates that the virial stress measures the momentum flux, not just the mechanical force between different material points, which is represented in the Cauchy stress. See Zhou (2003) and Cormier et al. (2001) for further discussions.

Similarly when Lagrangian coordinates are used, we define

$$\begin{aligned}
\widetilde{\rho}(\mathbf{x}^0, t) &= \sum_i m_i \delta(\mathbf{x}^0 - \mathbf{x}_i^0), \\
\widetilde{\mathbf{v}}(\mathbf{x}^0, t) &= \sum_i \mathbf{v}_i(t) \delta(\mathbf{x}^0 - \mathbf{x}_i^0), \\
\widetilde{\mathbf{q}}(\mathbf{x}^0, t) &= \sum_i m_i \mathbf{v}_i(t) \delta(\mathbf{x}^0 - \mathbf{x}_i^0), \\
\widetilde{e}(\mathbf{x}^0, t) &= \frac{1}{2} \sum_i \left[m_i \mathbf{v}_i^2 + \sum_{j \neq i} \phi(\mathbf{x}_i(t) - \mathbf{x}_j(t)) \right] \delta(\mathbf{x}^0 - \mathbf{x}_i^0)
\end{aligned} \tag{7}$$

and

$$\begin{aligned}
\widetilde{\boldsymbol{\sigma}}_{\alpha\beta}(\mathbf{x}^0, t) = & -\frac{1}{2} \sum_{i \neq j} f_\alpha(\mathbf{x}_i - \mathbf{x}_j)(x_{i\beta}^0 - x_{j\beta}^0) \\
& \times \int_0^1 \delta(\mathbf{x}^0 - (\mathbf{x}_j^0 + \lambda(\mathbf{x}_i^0 - \mathbf{x}_j^0))) \, \mathrm{d}\lambda, \\
\widetilde{\mathbf{j}}(\mathbf{x}^0, t) = & \frac{1}{4} \sum_{i \neq j} (\mathbf{v}_i + \mathbf{v}_j) \cdot \mathbf{f}(\mathbf{x}_j - \mathbf{x}_i)(\mathbf{x}_i^0 - \mathbf{x}_j^0) \\
& \times \int_0^1 \delta(\mathbf{x}^0 - (\mathbf{x}_j^0 + \lambda(\mathbf{x}_i^0 - \mathbf{x}_j^0))) \, \mathrm{d}\lambda,
\end{aligned} \tag{8}$$

then we have

$$\begin{aligned}
&\partial_t \widetilde{\mathbf{q}} - \nabla_{\mathbf{x}^0} \cdot \widetilde{\boldsymbol{\sigma}} = 0, \\
&\rho_0 \partial_t \widetilde{e} + \nabla_{\mathbf{x}^0} \cdot \widetilde{\mathbf{j}} = 0.
\end{aligned} \tag{9}$$

Again one may compute the average of the stress over certain domain Ω_0 (in the reference coordinate):

$$\frac{1}{|\Omega_0|} \sum_{i<j} \mathbf{f}(\mathbf{x}_j - \mathbf{x}_i) \otimes (\mathbf{x}_i^0 - \mathbf{x}_j^0) c_{ij}.$$

This agrees with the virial expression of Piola–Kirchhoff stress.

Physically one can think of Eqs. (2) and (3) as being the ensemble averages of Eqs. (5) and (9). Near crystal defects or free surface, the expressions in Eqs. (8) and (6) might not provide an accurate measure of the stress or the energy flux, as has been discussed in Zimmerman et al. (2004). However the conservation laws (5) and (9) always hold.

Remark. Note that one can rewrite the energy flux as

$$\widetilde{\mathbf{j}} = -\mathbf{v} \cdot \widetilde{\boldsymbol{\sigma}} + \widetilde{\mathbf{j}}_0$$

with $\mathbf{v}$ being the mean velocity and $\widetilde{\mathbf{j}}_0$ the heat flux, which has the same expression as $\widetilde{\mathbf{j}}$ but with $\mathbf{v}_j$ replaced by $\mathbf{v}_j - \mathbf{v}$. With this modification, one can always perform MD simulations with zero total momentum because the pressure (or stress) is invariant under translation.

The above discussion suggests a new coupling strategy in the HMM framework at the level of fluxes: the macroscopic variables can be used as constraints for the atomistic system, the needed constitutive data (the fluxes), can be obtained from the atomistic model via ensemble/time averaging after the microscale system equilibrates. In the following section, we will show how this strategy can be implemented.

3. Type B problem—atomistic-based constitutive modeling

Traditionally continuum models of solids are based on empirical constitutive relations. Linear elasticity is a good example of such empirical models, in which the atomistic information is lumped into very few parameters, the elastic moduli, that depend on the symmetry properties of the material. However, in many cases the accuracy of these empirical constitutive relations are insufficient, and one way to improve the accuracy is to use constitutive information obtained directly from atomistic models.

There are two ways of implementing such a procedure. The first is to assume a functional form for the constitutive relation and use precomputed data from the atomistic model to determine the parameters. This approach is preferred if the constitutive relation depends on few parameters so that a limited set of precomputed data is sufficient for constructing the constitutive model. The second approach is to compute the needed constitutive information "on the fly" from the atomistic model as the simulation proceeds, as in the Car–Parrinello method (Car and Parrinello, 1985). This approach is preferred if the constitutive relation depends on a large set of parameters so that precomputing becomes inefficient. The potential disadvantage of this approach is that redundant calculations might be performed in the course of extracting constitutive information using the microscale model. This problem can be reduced by adopting strategies that make use of the constitutive information that has already been computed, as in the semi-empirical methods discussed in E and Engquist (2002). The first approach is usually referred to as serial coupling. The second approach is usually referred to as concurrent coupling. In any case, a very important component in both approaches is to set up atomistic calculations so that information on constitutive relations can be obtained. In this section we will address this question. We will organize our discussion around concurrent coupling, since there are additional issues there that have to be addressed. But most of the proposed methodologies also apply to serial coupling.

3.1. Methodology

Following the HMM framework, we will discuss how to select the macroscale solver and how MD simulations are set up to provide the needed constitutive information.

For clarity, we restrict most of the discussions to one-dimensional continuum models (the atomistic models can be in any dimension). Extension to high-dimensional continuum models is mostly straightforward and will be briefly explained later.

3.1.1. Macroscale solver

Our basic macroscopic model is a set of conservation laws. Although there are a variety of methods available for solving conservation laws (LeVeque, 1992; Godlewski and Raviart, 1996), many of them involve computing the Jacobian of the flux functions, which dramatically increases the computational complexity in a coupled multiscale method when the constitutive relation has to be extracted from atomistic models. One exception is the central scheme of Lax–Friedrichs type, such as Nessyahu and Tadmor (1990) which is formulated over a staggered-grid. In the following we will focus on this macroscale solver. However, we should emphasize that the use of staggered grid is only a matter of convenience, not necessity.

For convenience, we rewrite the conservation laws in the generic form:

$$\mathbf{w}_t + \mathbf{f}_x = 0, \tag{10}$$

where $\mathbf{w}$ denotes the conserved quantities, and $\mathbf{f}$ is some (unknown) flux function. We first lay out a staggered grid as indicated in Fig. 1.

The first-order central scheme represents the solutions by piecewise constants, which are the average values over each cell:

$$\mathbf{w}_k^n = \frac{1}{\Delta x}\int_{x_{k-1/2}}^{x_{k+1/2}} \mathbf{w}(x, t^n)\,\mathrm{d}x.$$

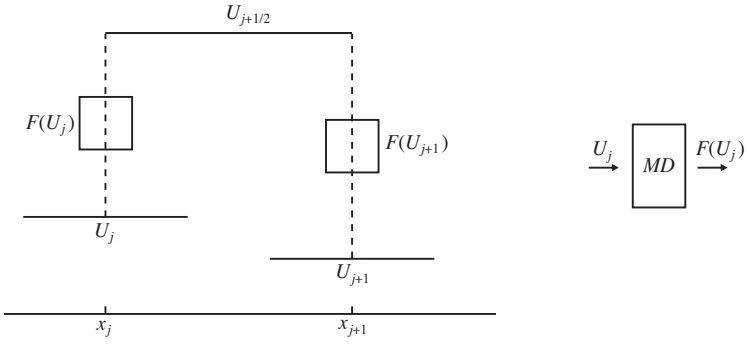

Fig. 1. A schematic illustration of the numerical procedure: starting from piecewise constant solutions $\{\mathbf{U}_j^n\}$, one integrates Eq. (10) in time and in the cell $[x_j, x_{j+1}]$. To estimate $\mathbf{F}$ at x_j, we perform a MD simulation using $\mathbf{U}_j^n$ as constraints. This is indicated in the picture by small boxes.

Here Δx is the size of the cell. Integrating Eq. (10) over $[x_j,\ x_{j+1}] \times [t^n,\ t^{n+1})$ leads to the following:

$$\mathbf{w}_{k+1/2}^{n+1} = \frac{\mathbf{w}_k^n + \mathbf{w}_{k+1}^n}{2} - \frac{\Delta t}{\Delta x}(\mathbf{f}_{k+1}^n - \mathbf{f}_k^n), \tag{11}$$

where

$$\mathbf{f}_k^n = \frac{1}{\Delta t}\int_{t^n}^{t^{n+1}} \mathbf{f}(x_k, t)\,\mathrm{d}t.$$

This is then approximated by numerical quadrature such as the mid-point formula. A simple choice is $\mathbf{f}_k^n \sim \mathbf{f}(x_k, t^n)$.

The stability of such schemes, which usually manifests itself in the form of a constraint on the size of Δt, can be easily appreciated from considering the adiabatic case when $\mathbf{f} = \mathbf{f}(\mathbf{w})$: if we choose the time step Δt small enough, the waves generated from the cell interface $\{x_{k+1/2}\}$ will not arrive at the grid points $\{x_k\}$ at the next time step, and therefore the solution as well as the fluxes at the grid points will not change until the next time step.

With this specific macrosolver, we illustrate the HMM procedure, which is shown schematically in Fig. 1. At each time step, scheme (11) requires as input the fluxes at grid point x_k. These flux values are obtained by performing local MD simulations that are constrained by the local macrostate variables (ρ, $\mathbf{q}$, E) (or ($\mathbf{A}$, $\mathbf{v}$, e) in Lagrangian coordinates). After the MD system equilibrates, we estimate the fluxes by time/ensemble averaging.

As is standard for hyperbolic problems, one can use piecewise linear representation of the solutions to achieve better accuracy,

$$\mathbf{w}(x) = \mathbf{w}_k + \partial_x \mathbf{w}_k (x - x_k), \quad x \in (x_{k-1/2}, x_{k+1/2}]. \tag{12}$$

Slope limiters can be used to suppress unphysical oscillations if necessary. For instance, a commonly used limiter is the 'minmod' limiter:

$$\partial_x \mathbf{w}_k = \mathrm{minmod}\left(\frac{\mathbf{w}_{k+1} - \mathbf{w}_k}{\Delta x}, \frac{\mathbf{w}_k - \mathbf{w}_{k-1}}{\Delta x}\right), \tag{13}$$

where the function

$$\mathrm{minmod}(t_1, t_2) = \tfrac{1}{2}(\mathrm{sgn}(t_1) + \mathrm{sgn}(t_2))(|t_1| + |t_2|)$$

is applied to each component. Other limiters can be found in standard textbooks (Le Veque, 1992; Godlewski and Raviart, 1996). A convenient second-order macroscale solver consists of two half-steps:

$$\mathbf{w}_k^{n+1/2} = \mathbf{w}_k^n - \frac{\Delta t}{2\Delta x}\,\partial_x \mathbf{f}_k^n,$$

$$\mathbf{w}_{k+1/2}^{n+1} = \frac{\mathbf{w}_k^n + \mathbf{w}_{k+1}^n}{2} + \frac{\Delta x}{8}(\partial_x \mathbf{w}_k^n - \partial_x \mathbf{w}_{k+1}^n) - \frac{\Delta t}{\Delta x}(\mathbf{f}_{k+1}^{n+1/2} - \mathbf{f}_k^{n+1/2}).$$

In the first half-step, the gradient for the flux $\mathbf{f}_k$ is again evaluated via a simple slope limiter, i.e.

$$\partial_x \mathbf{f}_k = \text{minmod}\left(\frac{\mathbf{f}_{k+1}-\mathbf{f}_k}{\Delta x}, \frac{\mathbf{f}_k-\mathbf{f}_{k-1}}{\Delta x}\right).$$

Generalization to high dimensions is straightforward. In the two-dimensional case with conservation laws:

$$\mathbf{w}_t + \mathbf{f}_x + \mathbf{g}_y = 0, \tag{14}$$

where the first-order scheme on staggered (rectangular) grid is given by

$$\begin{aligned}\mathbf{w}^{n+1}_{j+1/2,k+1/2} = {} & \frac{1}{4}(\mathbf{w}^n_{j,k} + \mathbf{w}^n_{j+1,k} + \mathbf{w}^n_{j,k+1} + \mathbf{w}^n_{j+1,k+1}) \\ & - \frac{\Delta t}{2\Delta x}(\mathbf{f}^n_{j+1,k} - \mathbf{f}^n_{j,k} + \mathbf{f}^n_{j+1,k+1} - \mathbf{f}^n_{j,k+1}) \\ & - \frac{\Delta t}{2\Delta y}(\mathbf{g}^n_{j,k+1} - \mathbf{g}^n_{j,k} + \mathbf{g}^n_{j+1,k+1} - \mathbf{g}^n_{j+1,k}).\end{aligned} \tag{15}$$

In our work, we often use the high-order central schemes developed by Nessyahu and Tadmor (1990).

3.1.2. Reconstruction

Next we discuss the steps involved in setting up the MD to estimate the local fluxes. The first step in setting up the MD simulation is to reconstruct MD configurations that are consistent with the local macrostate variables.

Given the local macroscopic state $\mathbf{A}, \mathbf{v}, E$, we first determine the shape of the MD cell from the local deformation tensor. This is illustrated in Fig. 2. Consider the situation of a Bravais lattice and let $\mathbf{E}$ be a basis for the undeformed cell. The new cell is generated by the basis vectors $\tilde{\mathbf{E}} = \mathbf{AE}$. This is equivalent to setting up a linear displacement field. The potential energy $\mathscr{U}$ of this configuration and the kinetic energy associated with the mean velocity is subtracted from the total energy E to give us the thermal energy, and this gives the temperature. Knowing the mean and

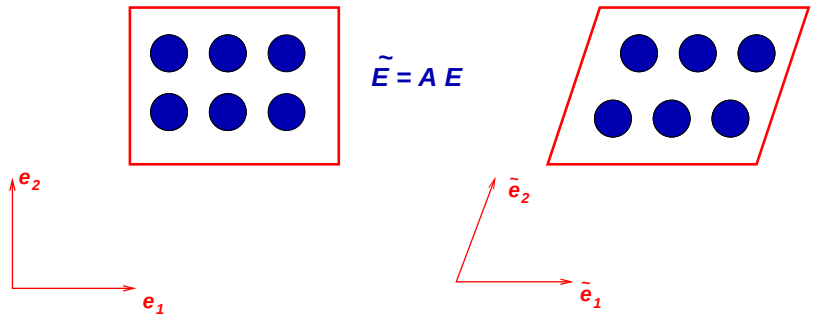

Fig. 2. Initializing the microscopic state: the MD cell is deformed according to the local deformation tensor.

variance of the velocity distributions, we initialize the particle velocities by the Maxwell–Boltzmann distribution.

We should remark that if the local relaxation time is very short, then there is not much difference in the performance of different initialization procedures, as long as the initial configuration has the correct crystal structure. However, as the relaxation time increases, there can be considerable advantage in using the previously computed microscopic state as the initial configuration for the new MD simulation. Of course the previously computed microscopic state has to be modified in order to be consistent with the current macrostate. This can be done as follows:

(1) the configuration is deformed linearly to be consistent with the current deformation gradient;
(2) the average velocity is rescaled to the current average velocity;
(3) the temperature is changed using the same procedure as discussed above to obtain the required total energy.

In the MD simulations, we use the standard Verlet method for MD with a neighbor list (Frenkel and Smit, 2002).

3.1.3. *Boundary conditions*

Boundary conditions have to be imposed on the microscopic system in order to guarantee consistency with the local macroscale variables. In the case when the system is homogeneous (constant mean velocity, temperature and deformation gradient), the most convenient boundary condition is the periodic boundary condition. The MD cell is first deformed according to the deformation gradient A (see Fig. 3) and periodically extended to the whole space.

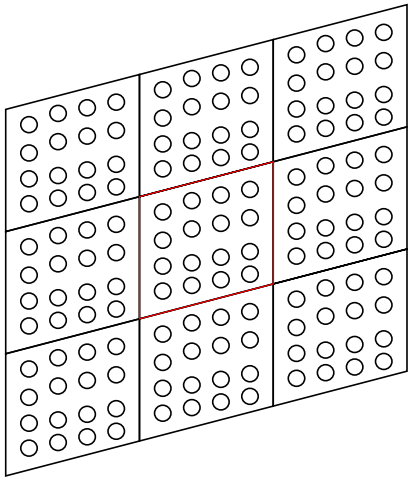

Fig. 3. Periodic boundary conditions: the MD cell is periodically extended to the whole space.

The periodic boundary condition excludes the possibility of accounting for inhomogeneous effects such as effects of thermal gradients, strain gradients, etc. These will be discussed in a future publication.

3.1.4. Estimating the data

From the MD data, we can compute the microscopic fluxes using the formulas in Eq. (8). The final step is to average the microscopic fluxes to obtain the fluxes needed by the macroscopic scheme.

The simplest approach is to perform a simple time average of the microscopic fluxes after the MD system is equilibrated. However we can often improve the quality of the averaging by using a more sophisticated kernel, for example,

$$\langle A\rangle_K = \lim_{t\to+\infty} \frac{1}{t}\int_0^t K\left(1-\frac{s}{t}\right)A(s)\,\mathrm{d}s, \quad K(\theta) = 1-\cos(2\pi\theta). \tag{16}$$

This kernel K gives less weight to the transient period and therefore faster convergence. In Fig. 4 we show a typical result of time averaging for pressure obtained from the molecular dynamics simulation and we compare the results from straightforward time averaging and averaging using the kernel $K(\theta)$. The introduction of the kernel obviously accelerates the convergence.

This kernel and more general kernels are discussed in Engquist and Tsai (in press) and Cancès et al. (2004).

In Fig. 4, we can see that for this example the macroscale fluxes can be reliably estimated after about 1000 MD times steps, independent of the size of the macro time step. This is a key feature of the method introduced here and HMM in general. By coupling the macro and micromodel at the level of data estimation, we automatically decouple the micro-time-scales from the macrotime scales. Other examples may require different number of microsteps. But still this is independent of the macro-time-scale.

The decoupling of micro- and macro-time-scales in the method proposed here is different from methods that are developed for modeling rare events (Voter and Chin, 1987). For the method proposed here, even though the MD simulation time is short compared to the macroscale time scale, it could still be very long compared with the micro-time-steps if the relaxation of the microscopic system involves overcoming substantial energy barrier.

How should we choose the size of the MD system and the duration of the MD simulation? The size of the atomistic system has to be carefully chosen. It should be as small as the accuracy requirement allows. Usually the correct size is determined beforehand by a number of test runs. Cormier et al. (2001) have shown a number of examples demonstrating the finite size effect. A series of numerical experiments have been conducted for systems of varying sizes $V = L^3$ to study the finite size effect. Plotted in Fig. 5 is a result on the finite size error. The exact value was obtained from a simulation for large L. For a given L, we measure the stress component τ_{11} by time averaging for sufficiently long time to eliminate the relaxation and sampling error. The error decays as the system size increases, consistent with the naive guess $L^{-1.5}$ from the central limit theorem.

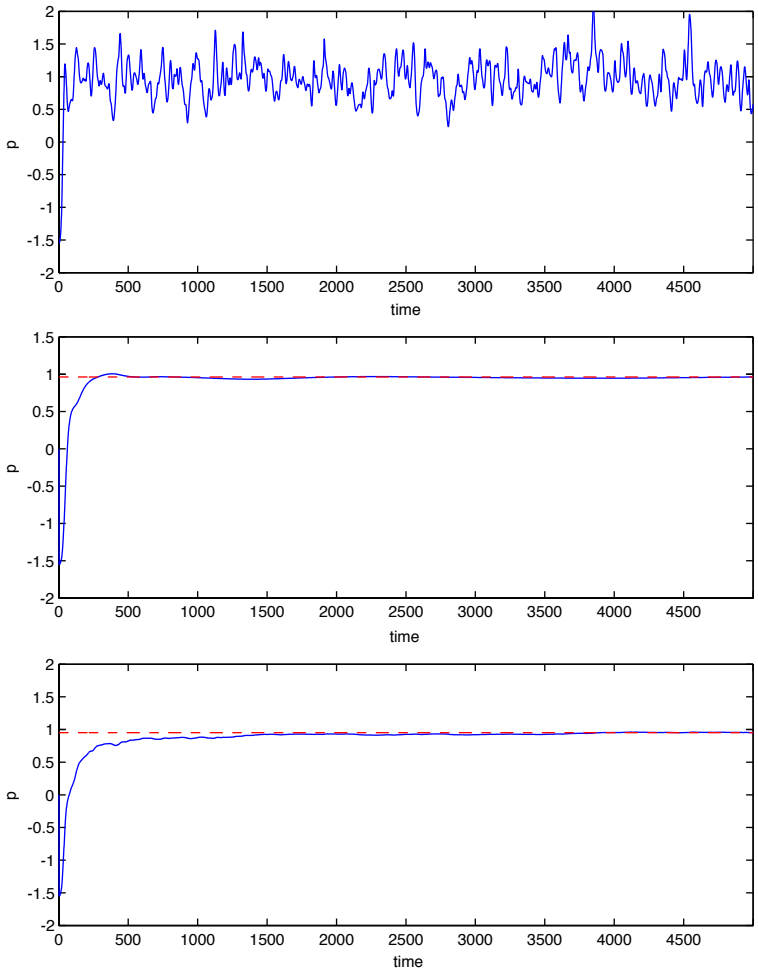

Fig. 4. Top: data from MD, middle: weighted average using the kernel K, and bottom: straightforward time average. The x-axis indicates the MD time steps. For better view, the desired values are also plotted (in dashed lines). This figure indicates that the kernel (16) provides slightly faster convergence to the expected value.

In the multiscale setting, more factors have to be taken into consideration to balance the overall accuracy and efficiency. Ideally one should develop systematic procedures for change the size of the MD system as well as systematic stopping criteria for MD, once the necessary macroscale data have been estimated to the desired accuracy. This is not yet done, and remains to be a general problem for HMM. Currently we adopt a more ad hoc strategy by performing some numerical experiments in the precomputing stage.

An error analysis of the overall method can be found in E and Li (2004).

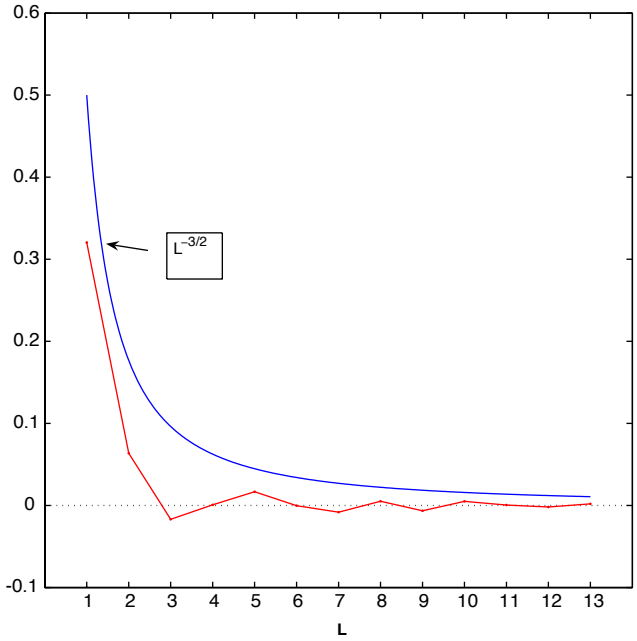

Fig. 5. Error due to finite size effect, plotted together with the $L^{-1.5}$ curve. In all the experiments, we consider tensile strain $A_{11} = 0.01$ on an aluminum system, and estimate the stress component σ_{11} by time averaging.

3.2. Numerical results

3.2.1. Shock propagation in a two-dimensional Lennard–Jones system

In this example, the system is described at the atomistic level by a two-dimensional Lennard–Jones potential:

$$\phi(r) = 4\varepsilon\left(\left(\frac{\sigma}{r}\right)^{12} - \left(\frac{\sigma}{r}\right)^{6}\right).$$

All the results shown below are expressed in terms of the reduced units, e.g. $\sqrt{m/\varepsilon}$ for the velocity, ε/k_B for the temperature, etc. The initial condition is set up as follows: For the $x<0$ half plane, we impose an uniform deformation gradient $A_{1,1} = 0.99$, and for the other half plane, the deformation gradient is zero. The system starts from zero velocity and uniform temperature: $T = 0.3$. From the continuum viewpoint, this is an example of the popular Riemann problem.

Evidently at the continuum level, we may assume that the solution is one dimensional. The continuum equations then reduce to

$$\begin{aligned} &\partial_t \varepsilon_{11} - \partial_x v_1 = 0, \\ &\rho_0 \partial_t v_1 + \partial_x \sigma_{11} = 0, \\ &\rho_0 \partial_t e + \partial_x (\sigma_{11} v_1) = 0. \end{aligned} \tag{17}$$

We apply the multiscale procedure discussed above to this problem with the second order central scheme as the macroscale solver. The numerical results are shown in Fig. 6. At $t>0$, one observes two shocks separated by a contact discontinuity (the velocity is continuous at the contact discontinuity).

Notice that the solution $\mathbf{u}(x,t)$ to the conservation laws is self-similar: for any $\lambda>0$, $\mathbf{u}(\lambda x,\lambda t)$ is also a solution if $\mathbf{u}(x,t)$ is. This suggests a way of verifying the numerical solution of the multiscale method: we can perform a small scale full

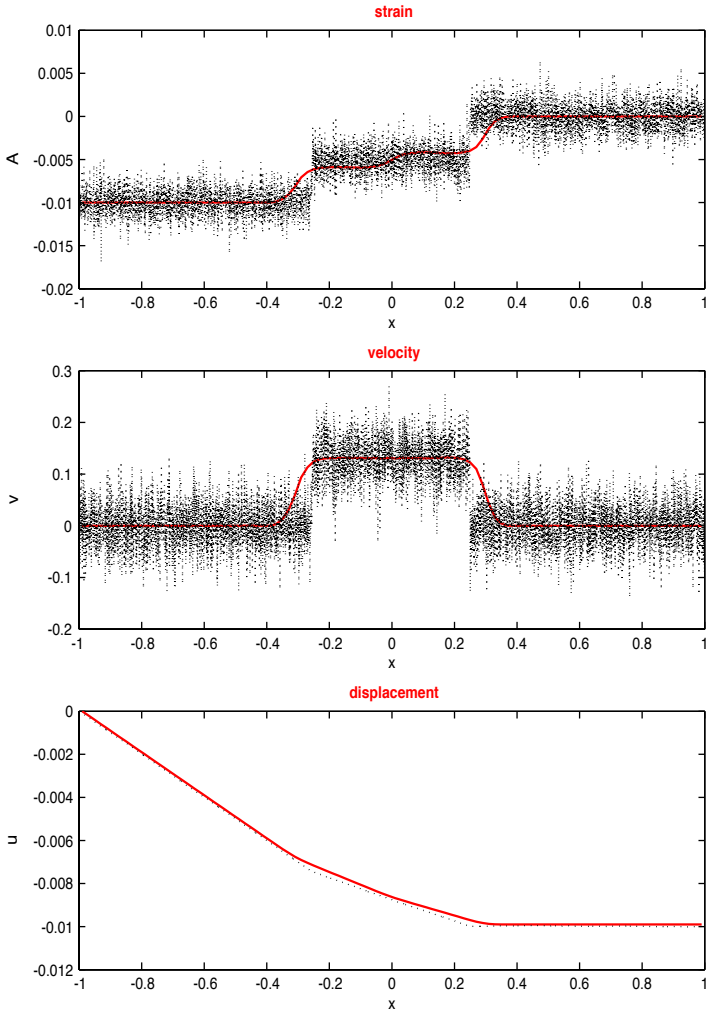

Fig. 6. Numerical test on shock formation and propagation. Two hundred macrogrid points are used and each local MD simulation consists of 40×10 atoms and 10^4 steps of time integration. The solution is displayed after 40 steps of integration over macro-time-steps. Solid line: computed solution; dashed line: full atom simulation (one realization). Top: strain, middle: velocity, bottom: displacement.

atomistic simulation and then rescale the MD solutions to the scale of the multiscale solution. This rescaled MD solution can then be compared with the HMM solution. The result is shown in Fig. 6. We see that for velocity and strain, the MD solution fluctuates around the HMM solution, as expected. But for the displacement field, which is an integrated quantity, we see direct agreement.

3.2.2. Thermal expansion

In the second example, we study the effect of thermal expansion. Our atomistic model is a three-dimensional Lennard–Jones solid in a face-centered cubic (FCC) lattice. We set up the example so that the macroscale behavior is two-dimensional. Initially the material is at rest with homogenous temperature distribution $T \equiv 0.1$. We then increase the temperature in the middle instantaneously to $T = 0.4$. This results in a thermal expansion that propagates outward. We solve Eq. (3) by the two-dimensional central scheme described above. In Fig. 7 we display the numerical results for the temperature distribution as well as the velocity field. One clearly observes that the material is expanding outward as the heat is spread out.

4. Dealing with isolated defects—type A problems

We now turn to another class of problems that can be treated using multiscale methods, the problem of isolated defects. These are type A problems according to the classification in E and Engquist (2002). Solids often contain a variety of defects, such as vacancies, dislocations, twin boundaries and grain boundaries. To a large extent, the structure and dynamics of these defects determine the properties of the solid.

A common idea for the multiscale modeling of defects is to use atomistic models near defects and continuum models away from defects, e.g. in a domain decomposition framework. MAAD is a good example of such an approach. The HMM philosophy, on the other hand, suggests a strategy that is closer to the strategy of adaptive model refinement (Garcia et al., 1999; Oden and Vemaganti, 2000).

4.1. Adaptive model refinement: methodology

The idea of adaptive model refinement is to start with a macroscale model on a macrogrid (which might be locally refined) in the entire computational domain and couple with a more refined model locally near the defects. For the present problem, the macroscale model is the same as before, namely the conservation laws. The macroscale solver can also be chosen as before, i.e. central type of finite volume schemes. But when it comes to computing the fluxes, the cells (more precisely, the cell boundaries where flux evaluation is carried out) are divided into two types: cells that contain defects and cells that do not contain defects. In cells that do not contain defects we evaluate the fluxes using either empirical constitutive relations or the

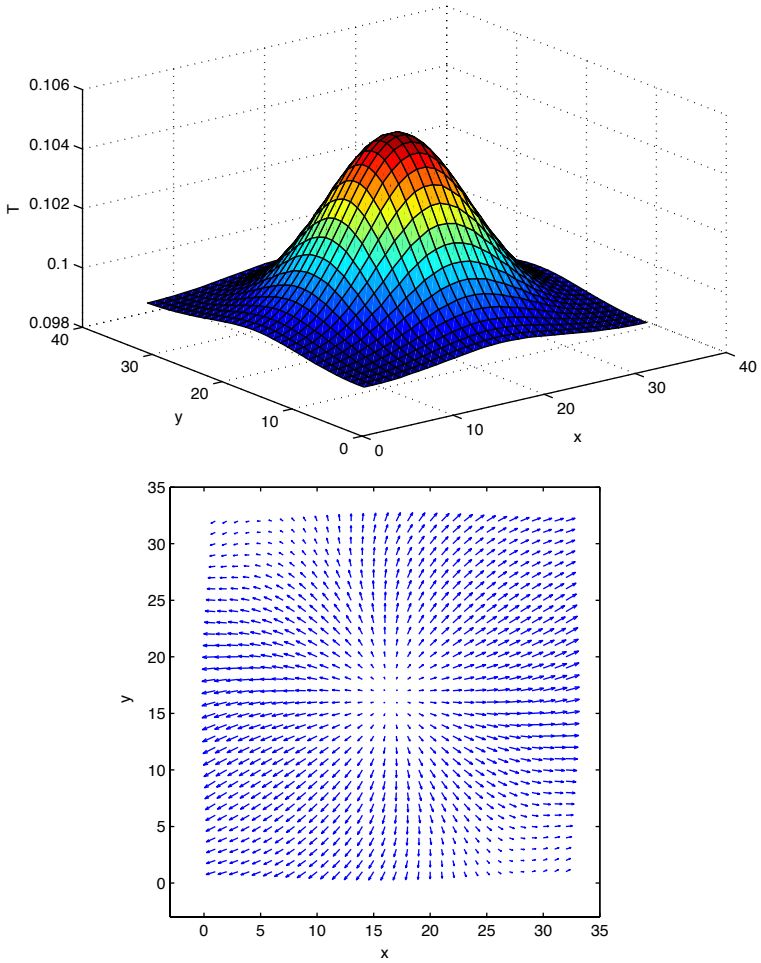

Fig. 7. Thermal expansion: temperature distribution (top) and the velocity field (bottom). The macromesh consists of 36×36 grid points. Each MD cell contains $36 \times 36 \times 3 \times 4$ atoms, and the system is evolved for 10^4 time steps.

method discussed in the previous section. In cells that do contain defects we compute the fluxes using MD.

To formulate the procedure of coupling MD with the continuum models near defects, we distinguish two different situations depending on whether there is scale separation between the time scale for the dynamics of the defects and the time scale for the local relaxation of the defect structure. We denote the former by T_{d} and the latter by T_{r}.

If T_{d} is much larger than T_{r}, as is the case in the example of one-dimensional elastic bar discussed below, we can extend the macroscale model

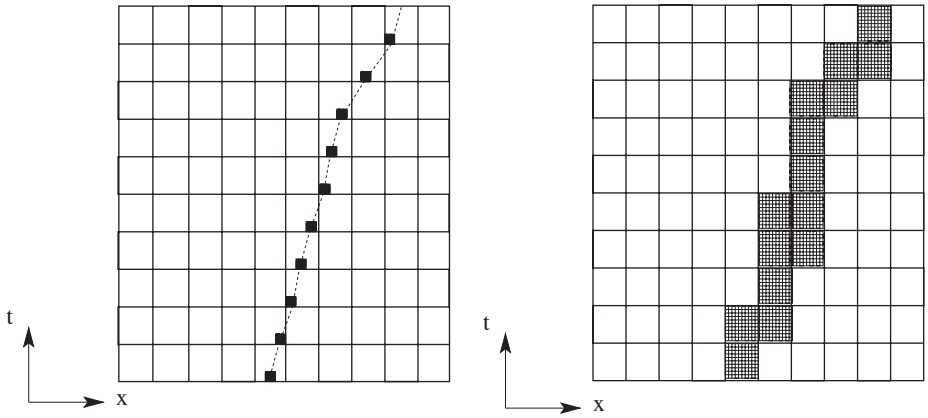

Fig. 8. Schematic of the adaptive modeling refinement. The top figure shows the case where $T_r \ll T_d$. The MD simulations are reinitialized at every macro-time-step. The dashed lines represents the interface. The bottom figure shows the other case where T_r and T_d are comparable. Here one has to keep track the local defect structure for all time.

to include the moving speed of the defect. The macroscale scheme then contains two components: a solver for the conservation laws (a central type finite volume scheme or discontinuous Galerkin method) and defect tracking. The data to be measured from MD include the fluxes, the defect velocity and the local environment of the defect. This procedure naturally decouples the two time scales T_r and T_d.

If T_d is comparable to T_r, then the time history of the defect structure is important for its future dynamics. In this case we will have to track the entire history of the local atomistic structures near the defect. There is no decoupling of time scales since there is no time scale separation. This situation often arises when dealing with small-size materials. Fig. 8 illustrates the procedure for both of these cases.

4.2. Defect tracking

When $T_r \ll T_d$, we can extract information on the dynamics of the defect from *local* MD simulations, and use it to advance the defects over macro-time-steps. At the same time the macrosolver needs to be modified near the interface to take into account the defect structure. This defect tracking procedure is similar in spirit to the front tracking algorithms in computational fluid dynamics (Glimm et al., 2002, 1998), except that the speed of front is not obtained from macroscopic jump conditions but from molecular dynamics.

The defect tracking procedure is illustrated in Fig. 9. Here we only show how to treat surface defect, and we restrict the discussion to the one-dimensional case. Suppose that at time t^n the interface is located at z^n, which is inside the kth cell. Assume that $z^n > x_k$ and without loss of generality, assume that the propagation

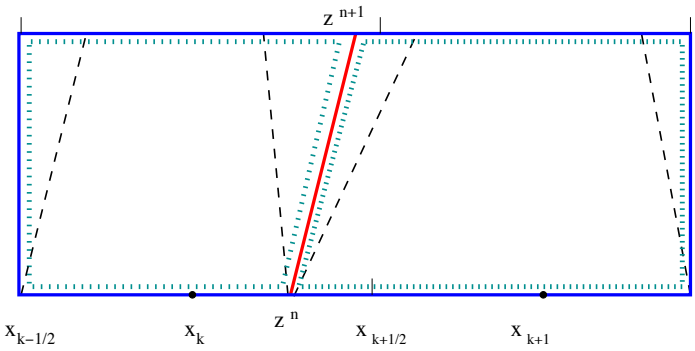

Fig. 9. A schematic demonstration of the defect tracking procedure. z^n represents the current interface location. The dotted line indicates the domain over which the PDEs (3) are integrated. The dashed line represents elastic waves generated from the Riemann problem, and the solid line in the middle indicates the interface.

speed $c_n \geqslant 0$. Let

$$I_l^n = \{(x,t)|x \in (x_{k-1/2}, z^n + c_n t], t \in (t^n, t^{n+1}]\},$$
$$I_r^n = \{(x,t)|x \in (z^n + c_n t, x_{k+3/2}], t \in (t^n, t^{n+1}]\}.$$

We also use $\mathbf{w}_{k-1}^n$ and $\mathbf{w}_k^n$ to represent the numerical solutions (cell average) on $(x_{k-1/2}, z^n]$ and $(z^n, x_{k+3/2}]$, respectively.

(1) Remember that our basic macroscale model is still a system of conservation laws, integrate a generic conservation law $\partial_t \mathbf{w} + \partial_x \mathbf{f} = 0$ over the region I_l^n and I_r^n, we get:

$$(z^{n+1} - x_{k-1})\mathbf{w}_{k-1/2}^{n+1} - \mathbf{w}_{k-1}^n \Delta x/2 - \mathbf{w}_k^n (z^n - x_{k-1/2}) + (\mathbf{f}^- - c_n \mathbf{w}^-)\Delta t - \mathbf{f}_{k-1}^n \Delta t = 0$$

and

$$(x_{k+1} - z^{n+1})\mathbf{w}_{k+1/2}^{n+1} - \mathbf{w}_{k+1}^n (x_{k-1/2} - z^n) + \mathbf{f}_{k+1}^n \Delta t - (\mathbf{f}^+ - c_n \mathbf{w}^+)\Delta t = 0.$$

Here, $\mathbf{w}^\pm$ and $\mathbf{f}^\pm$ denote the macrostates on the right/left of the interface and the corresponding fluxes. From the well-known Rankine–Hugoniot condition, we should have

$$\mathbf{f}^+ - c_n \mathbf{w}^+ = \mathbf{f}^- - c_n \mathbf{w}^-. \tag{18}$$

(2) In order to predict the moving speed of the interface, c_n, and estimate the data $\mathbf{f}^+, \mathbf{f}^-, \mathbf{w}^+, \mathbf{w}^-$, which are needed to advance the system to the next macro-time-step, we perform a local MD simulation at the interface. The macrostates $\mathbf{w}_{k-1}^n$ and $\mathbf{w}_k^n$ are used to initialize the atomistic system, and to impose boundary conditions. The results of such simulations are analyzed to estimate the quantities we need.

The first step is to locate the interface. Notice that the Riemann problem has self-similar solutions, i.e., the solutions can be written as $\mathbf{u}(x,t) = \mathbf{W}(\eta), \eta = x/t$.

Therefore, we can divide the x–t domain into a number of zones,

$$Z_l = \{j | \eta_l < x_j/t \leqslant \eta_{l+1}\},$$

for a set of discrete values $\{\eta_l\}$. Since a priori we know the range of the solution at different sides, e.g. the order parameters (in the case of phase transformation, it can be identified by the values of the strain), we can easily detect the zone, say Z_m that contains the interface. We then estimate the quantities in Eq. (18) in the adjacent zones Z_{m-1} and Z_{m+1} by space/time average. Since Eq. (18) should be satisfied across the phase boundary, we select the speed c that best fits the jump condition (e.g. by least-square procedure).

In higher dimensions, the interface is represented by piecelinear curves or surfaces. The evolution of the interface is determined by a one-dimensional finite difference solver which involves the left and right states at the two sides the interface (Glimm et al., 1998). A library has been built which offers code for public access FronTier (http://galaxy.ams.sunysb.edu/FTdownload/). Extending this procedure to dealing with high co-dimensional defects such as point defects and dislocations still remains to be done.

4.3. Boundary conditions

Since the local MD system is no longer homogeneous, we need to modify the boundary condition that needs to be imposed on the MD system. Here we propose a simple boundary condition using the idea of border regions. For other related work on boundary conditions, we refer to Cai et al. (2000) and E and Huang (2001).

The first step is to extend the atomistic system by appending atoms to the border of the MD simulation cell. The border region is divided into bins as indicated in Fig. 10.

Next we define macroscale variables, namely displacement, velocity and temperature, on the bins by interpolating from their values on the macrogrid. We denote these continuum values at the boundary by $(\mathbf{u}_b, \mathbf{v}_b, T_b)$.

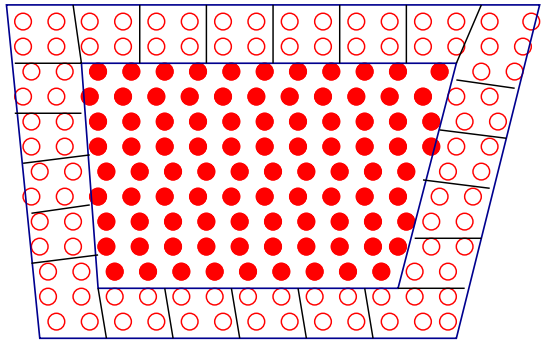

Fig. 10. Boundary conditions imposed on the atomistic system: the border region is divided into bins and Nose–Hoover is applied to each bin.

To obtain the boundary condition for MD, we separate out the mean from the fluctuating part, i.e. we rewrite the position and velocity of the atoms in the border region as

$$\mathbf{x}_j = \mathbf{x}_j^{(0)} + \mathbf{x}_j^{(1)}, \quad \mathbf{v}_j = \mathbf{v}_j^{(0)} + \mathbf{v}_j^{(1)}.$$

The macrocomponents, $\mathbf{x}_j^{(0)}$ and $\mathbf{v}_j^{(0)}$, are computed from $\mathbf{u}_b$ and $\mathbf{v}_b$, by interpolation if necessary. For the *micropart*, $\mathbf{x}_j^{(1)}$ and $\mathbf{v}_j^{(1)}$, we apply Nosè Hoover thermostat on each bin using temperature values from T_b, again using interpolation if necessary.

Various validation studies were conducted on this form of boundary condition. Here we report one result: the validation of Fourier law. The experiments are done on a $40 \times 40 \times 5$ aluminum system with EAM potential (Ercolessi and Adams, 1994). The temperature at the boundary is determined by linear profile with a specified temperature gradient ∇T and an average value. Fourier law states that

$$\mathbf{j} = -\kappa \nabla T$$

with κ being the heat conductivity. The boundary condition described above was used with $\mathbf{u}_b = 0, \mathbf{v}_b = 0$. A temperature gradient is imposed by different values of T_b at the two ends. In Fig. 11 we show the results from a series of numerical experiments

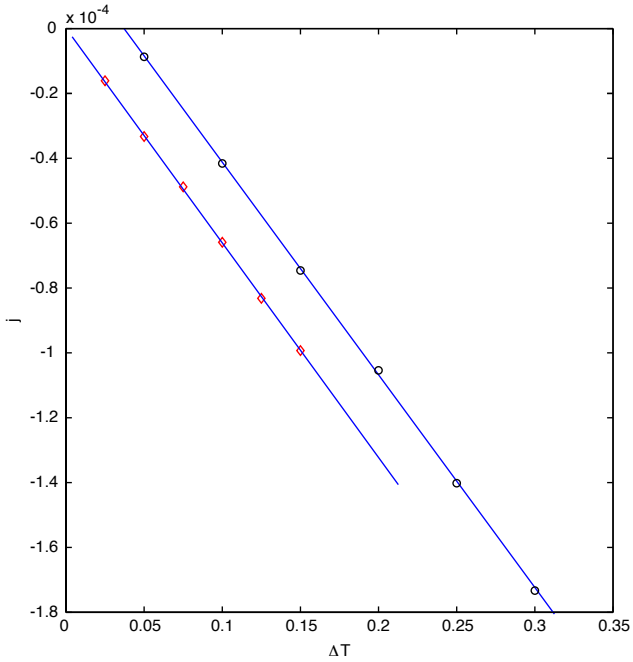

Fig. 11. Numerical experiment to test the Fourier law. 'o' and '◇' are the two components of $\mathbf{j}$, j_1 and j_2, respectively.

with different temperature gradient applied. One can clearly see the linear dependence of the heat flux on the gradient. Furthermore by linear fitting we have estimated the heat conductivity from these data. The average temperature of the system is 100 K, and the thermal conductivity is approximately $\kappa = 250$ (W/m/K), which agrees reasonably well with experimental data $\kappa = 234$ (W/m/K).

A key issue about MD boundary conditions is the reflection of phonons at the boundary. To test this, we used the boundary condition described above on the Frenkel–Kontorova model studied in this context in E and Huang (2001, 2002). Our results agree very well with those of E and Huang (2001, 2002).

4.4. Phase transformation

Next we apply the methods we have developed to study phase transformation in solids. Under stress or temperature change certain materials undergo phase transformation. A typical example is martensitic transformation, in which the material transforms from the more symmetric austenite phase to a less symmetric martensite phase. In the process of this transformation, the material displays a variety of microstructures. Much work has been done to understand these structural phase transformation, both at the atomistic and continuum level (Ball and James, 1992; Luskin, 1996; Li, 2001; Pinsook and Ackland, 2000; Becquart et al., 1993). For static problems, the Ball–James continuum theory (Ball and James, 1987, 1992) works with a postulated free energy function which below the transition temperature must have multiple minima due to the presence of several stable variants which are related to each other by symmetry. A consequence of this is that the variational problem does not have a minimizer. Nevertheless, it has been shown that the minimizing sequences contain valuable information on the microstructure. This has also motivated some very interesting numerical work (see e.g. Luskin, 1996; Li, 2001).

The situation for dynamics appears to be quite different. There at the continuum level it seems necessary to introduce additional mechanism as in the work of Slemrod (1983), or constitutive relation, called the kinetic relations, for the dynamics of the phase boundary, as is done in the work of Abeyaratne and Knowles (1991) and Purohit and Bhattacharya (2003). It is therefore of interest to understand the atomistic origin of these kinetic relations.

We will start with an investigation of a one-dimensional model which reflects a number of typical features in more general structural phase transformation. This simple model has inspired a great deal of work on the understanding of the energetics and kinetics of phase transformations (Abeyaratne et al., 2000; Abeyaratne and Knowles, 1991; Bhattacharya, 2003; Truskinovsky and Vainchtein, 2003; Purohit and Bhattacharya, 2003). We will present a defect tracking method to resolve the dynamics of the phase boundary, which bypasses empirical mobility laws. The phase boundary is reconstructed and evolved by a local atomistic simulation for short time, and we extract the necessary data in order to evolve the phase boundary to the next macro time step. Finally we apply this procedure to study twin boundary dynamics in a Ni–Al alloy system.

4.4.1. A simple one-dimensional model

The simplest model that exhibits phase transformation is a one-dimensional elastic bar, which can be modeled at the microscopic level by a chain of atoms connected by springs:

$$m\ddot{x}_j = \phi'(x_{j+1}(t) - x_j(t)) - \phi'(x_j(t) - x_{j-1}(t)), \tag{19}$$

where ϕ is the potential of the springs. The initial position of the jth atom is denoted by x_j^0.

To study phase transformation, we assume that the spring energy has a bi-stable form. For example:

$$\phi(r) = \begin{cases} \dfrac{1}{r} + r^2/2, & 0 < r \leqslant 1, \\ \dfrac{1}{2}r^2 - r + 2, & 1 < r \leqslant 2, \\ 5r - r^2 - 4, & 2 < r \leqslant 3, \\ \dfrac{19}{2} + \dfrac{1}{2}r^2 - 4r, & r > 3. \end{cases} \tag{20}$$

The two wells at $r = 1, 4$ represent the two different metastable states.

To investigate the dynamics of the phase boundary, we perform the following numerical simulation. Initially the particles are at rest and are equally spaced with distance $r = 1$, i.e. in the first well. Then we start to pull the left-most particle with a constant speed. The dynamics that emerges is shown in Fig. 12. First of all, a sound wave is generated that propagates to the right. If the pulling speed is above some critical value, the particles will have enough kinetic energy to overcome the potential barrier and jump to the second well. This results in a phase boundary that propagates to the right.

To illustrate the application of the multiscale method on this problem, consider the following example. Initially the macroscopic state of the system is described by two constant states separated by a phase boundary: the state on the left $(A, v, e) = (4.0277, -0.9977, 2.7734)$ corresponds to the second well and the state on the right $(A, v, e) = (1.0, 0, 1.5)$ corresponds to the first well. These two states are obtained from the previous experiments. Meanwhile the system is pulled from the right at a constant speed $v = 0.4$, which will create an additional elastic wave going to the left. The boundary conditions $\partial_x v = 0$, $\partial_x T = 0$ are applied during the simulation.

As the system is being pulled from the right, an elastic wave is generated at the right boundary and propagates to the left. The phase boundary in the middle propagates to the right. A right-moving weak shock is also generated at the phase boundary. At a later time the shock waves from the right impinges on the phase boundary. The shock-phase boundary interaction generates a reflected and a transmitted shock, and at the same time changes the speed of the phase boundary. As discussed in Section 3.2, due to the simple setup, it is feasible to compare the results of the multiscale method to that of a direction MD simulation. The MD

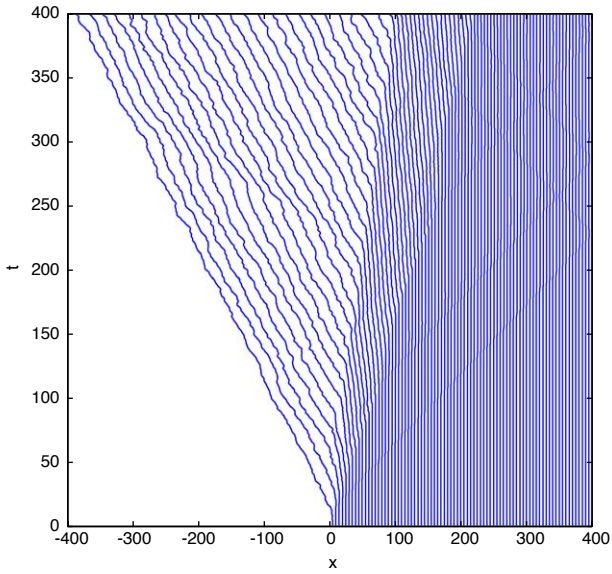

Fig. 12. Particle trajectory of the one-dimensional chain simulation: initially all the particles are at rest, with local strain in the first well. Then we start pulling the left end with a constant speed $v = -1.0$. A phase boundary and a sound wave are clearly observed.

system is set up in a similar way, and rescaled properly for the comparison. This is shown in Fig. 13.

In this simulation we have used 400 macrogrid points and the system is advanced in time for 100 steps with $\Delta t/\Delta x = 0.05$. In each local MD system around the phase boundary, an atomistic system consisting of 1000 atoms is evolved for 1000 time steps. The numerical results are shown in Fig. 14.

4.4.2. Twin boundary dynamics in Ni–Al alloy

Next we apply the multiscale method with defect tracking to study the dynamics of twin boundary in a $Ni_{62.5}Al_{37.5}$ alloy. As the atomistic model, we use the EAM potential developed by Voter and Chen (1987), which is specifically designed for Ni–Al alloys. At this percentage twin boundaries have been observed both experimentally (Chakravorty and Wayman, 1976; Nishiyama, 1978) and in atomistic simulations (with this EAM potential) (Becquart et al., 1993). In particular the EAM potential has predicted a tetragonal structure with three variants. The corresponding strain matrices can be written as

$$U_1 = \begin{pmatrix} \eta_1 & 0 & 0 \\ 0 & \eta_2 & 0 \\ 0 & 0 & \eta_2 \end{pmatrix}, \quad U_2 = \begin{pmatrix} \eta_2 & 0 & 0 \\ 0 & \eta_1 & 0 \\ 0 & 0 & \eta_2 \end{pmatrix}, \quad U_3 = \begin{pmatrix} \eta_2 & 0 & 0 \\ 0 & \eta_2 & 0 \\ 0 & 0 & \eta_1 \end{pmatrix}. \tag{21}$$

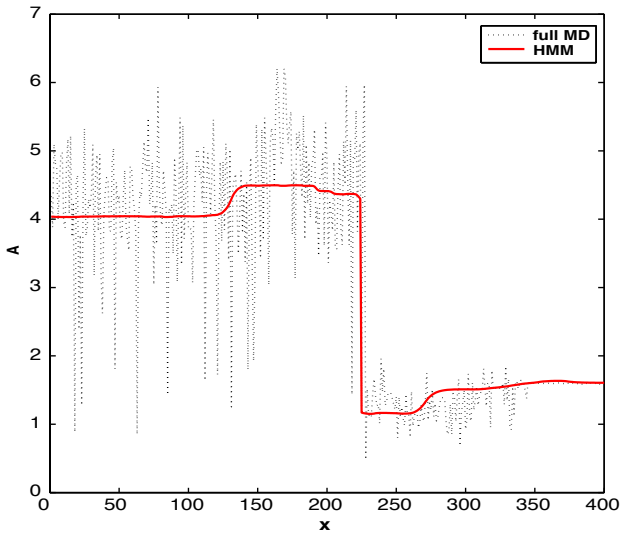

Fig. 13. Comparison of the multiscale solution with a full atomistic simulation. Dotted line: instantaneous strain from the full MD simulation; solid line: mean strain computed with our multiscale method.

We choose the cubic structure with lattice constant $a_0 = 2.871\,\text{Å}$ as the reference configuration. The parameters η_1 and η_2 can be thought of as being the stretch along the principal axis illustrated in Fig. 15. The values of these parameters are obtained from MD simulation: $\eta_1 = 1.2263$ and $\eta_2 = 0.9061$.

To form a compatible interface between two martensitic variants the deformation gradient $\mathbf{A}_1$ and $\mathbf{A}_2$ have to satisfy the relation:

$$\mathbf{A}_2 - \mathbf{A}_1 = \mathbf{a} \otimes \mathbf{n}, \tag{22}$$

where $\mathbf{n}$ is the normal vector of the interface.

For convenience we arrange the material so that the twin plane coincides with the y–z plane. The deformation corresponding to the undeformed variant I and variant II are:

$$\mathbf{A}_1 = \begin{pmatrix} \frac{\sqrt{2}\eta_1\eta_2}{\sqrt{\eta_1^2+\eta_2^2}} & 0 & 0 \\ \frac{\eta_1^2-\eta_2^2}{\sqrt{2(\eta_1^2+\eta_2^2)}} & \frac{\sqrt{\eta_1^2+\eta_2^2}}{\sqrt{2}} & 0 \\ 0 & 0 & \eta_2 \end{pmatrix}, \quad \mathbf{A}_2 = \begin{pmatrix} \frac{\sqrt{2}\eta_1\eta_2}{\sqrt{\eta_1^2+\eta_2^2}} & 0 & 0 \\ \frac{\eta_2^2-\eta_1^2}{\sqrt{2(\eta_1^2+\eta_2^2)}} & \frac{\sqrt{\eta_1^2+\eta_2^2}}{\sqrt{2}} & 0 \\ 0 & 0 & \eta_2 \end{pmatrix}. \tag{23}$$

This is depicted in Fig. 16.

Both experimental and theoretical studies of martensitic phase transformation (Ball and James, 1992) reveal that martensites tend to form twins in the process of phase transformation. But the dynamics has been much less discussed. Here we will use our multiscale method to investigate twin boundary dynamics. The movement of

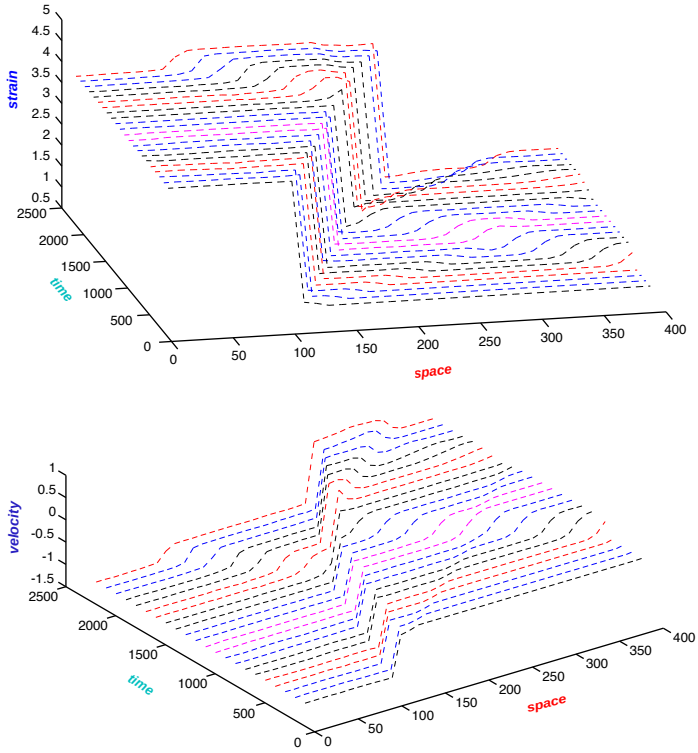

Fig. 14. Snapshots from the simulation: a phase boundary is present initially and the right end is pulled with constant speed. The shock wave and the phase boundary then collide. After the collision, a reflected and a transmitted wave are generated.

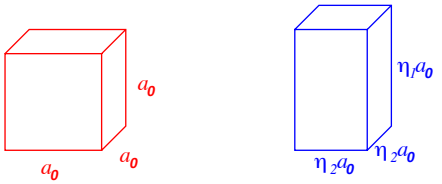

Fig. 15. Cubic phase and tetragonal phase for Ni–Al alloys.

the twin boundary can be driven by a shear stress applied at the boundary. In our experiment we set up the system with two variants with a single twin boundary in the middle. In order to generate a shear stress, we move the left boundary downward with a constant speed. The boundary on the right is fixed.

Since the twin boundary simply moves in x direction, and the continuum quantities do not have appreciable change in y and z directions, we can simplify the

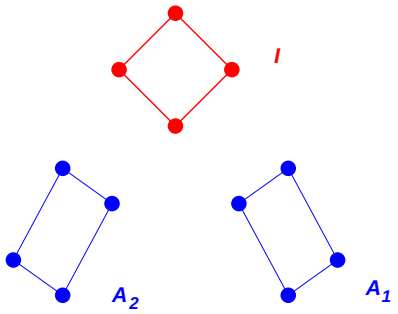

Fig. 16. Arrangement of the atoms in the cubic and tetragonal structure on the {0 0 1} plane: the deformation of the cubic phase is taken to be identity, while the two martensitic variants have deformation gradient given by Eq. (23).

continuum equations:

$$\begin{aligned}
&\partial_t A_{11} - \partial_x v_1 = 0,\\
&\partial_t A_{21} - \partial_x v_2 = 0,\\
&\rho_0 \partial_t v_1 + \partial_x \sigma_{11} = 0,\\
&\rho_0 \partial_t v_2 + \partial_x \sigma_{21} = 0.
\end{aligned} \tag{24}$$

For simplicity we have neglected the energy equation in this system. Instead we constrain the system to be at constant temperature. Other components of **A** are assumed not to change in time.

Away from the twin boundary, we perform local MD simulations to estimate the stress as we did in type B problems. Each such simulation involves $20 \times 20 \times 5$ atomic units and 2000 steps of time integration. The central (11) is applied on the macrogrid, which consists of 40 cells. In all the MD simulations the time step is taken to be $\delta t = 0.003$ ps. Near the twin boundary we apply the defect tracking technique to estimate the moving speed of the twin boundary and the local strain and stress. In each such MD calculation, we evolve a system with $120 \times 16 \times 16$ atomic units for 1200 time steps. To monitor the macroscale quantities, we set up two strain gauges near the phase boundary. In these gauges we sample the local strain, stress and velocity by averaging over a box consisting of $6 \times 6 \times 6$ atom units. From these sampled data, we can estimate the moving speed of the twin boundary from Eq. (18) by a least-square approximation. Periodic boundary conditions are applied in the y and z directions. At the left and right boundary, we apply boundary condition using the techniques discussed in Section 4.3. These boundary conditions help to maintain the strain and velocity on the both sides and prevent elastic waves to be reflected from the boundary and interfere with the twin boundary dynamics.

Fig. 19 shows the numerical results at the macroscale level after 40 macro-time-steps. As the twin boundary propagates, two elastic waves are generated and move away from the twin boundary.

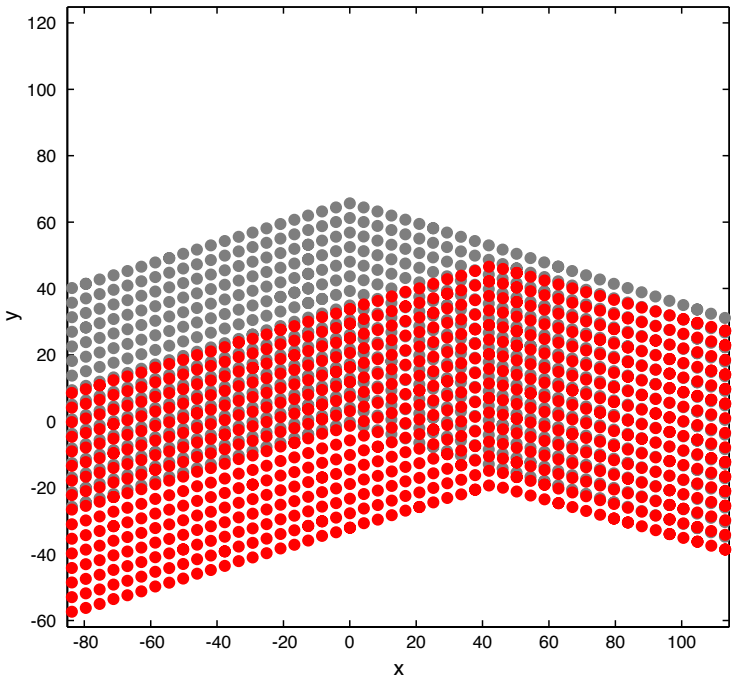

Fig. 17. Propagation of twin boundary under stress: shear stress is applied at the left boundary of the sample. The initial positions of the atoms are plotted in light color. The positions after 1.2 ps are plotted in dark color.

To better understand the mechanism of twin boundary propagation, we plot in Fig. 17 some results from the local MD at the twin boundary. We first select an arbitrary plane of atoms and examine their positions at the initial and final times of the MD. Different variants of the twin are easily identified as rectangle lattices with different orientation, as indicated in Fig. 16. We see that at the end of the MD, the twin boundary has clearly moved forward (in a layer by layer fashion).

Next we examine what happens on the twin plane as it propagates forward. For that purpose we plot the atomic positions of the atoms on the twin plane. Fig. 18 clearly suggests that the twin plane moves by a nucleation and propagation mechanism, very much similar to the mechanism of epitaxial growth of crystals. New variants are first nucleated and form islands on the twin plane. The edges of the islands then propagate out and induce the transformation on the whole plane. In analogy with epitaxial crystal growth, it is of interest to ask whether or when twin boundary dynamics proceeds via layer by layer growth or via island growth.

On the twin plane (y–z plane in Fig. 18), the atoms in light color belong to the layer behind the twin plane, which is in the original variant. In Fig. 1, most of the atoms on the plane are still in the first variant. They are identified by the fact that they are closer to their left neighbors in the next layer (the light color atoms). Those

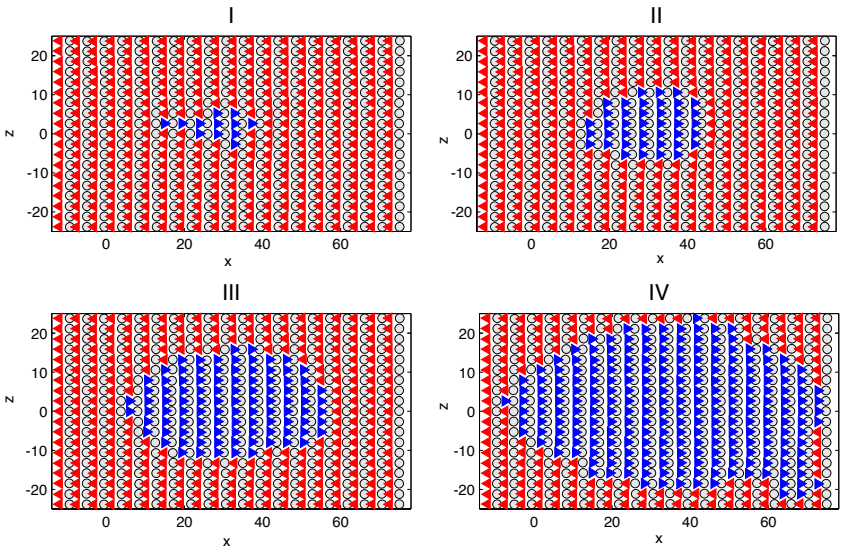

Fig. 18. Nucleation and propagation of new variant: '◁': atoms in the twin plane that are still in the original variant. '▷': atoms that have transformed to the new variant. Circle atoms belong to the layer next to the twin plane which are still in the original variant. They are used as reference atoms. Transformed atoms are closer to circle atoms at the right, whereas untransformed atoms are close to circle atoms at the left.

that are further away from their left neighbors are the new variants. One can see that the transformation will not proceed to the next layer until the current layer is completely transformed. The can be explained by the geometric constraint (22): if some new variants appear in the next layer before the current layer is fully transformed, the twin boundary will be tilted from a continuum point of view, which will then violate condition (22) (Fig. 19).

5. Conclusion

We have presented in this paper a fairly general simulation tool that couples efficiently atomistic and continuum models for crystalline solids. This method allows us to perform dynamic simulations with thermal effects, in which the atomistic models are used to model defects as well as constitutive relations. Even though we based our discussion on the framework of HMM, the specific algorithmic details are useful for any other coupling strategies, including serial coupling simulations in which the constitutive information is obtained in a precomputing step.

There are some relatively straightforward and not so straightforward extensions that one can envision. First of all, we concentrated on a finite volume macroscale solver in the present paper, but extension to finite element methods, particularly in a discontinuous Galerkin framework, should be possible. Next, one should be able to include the effect of viscous dissipation due to strain gradients. The strategy would

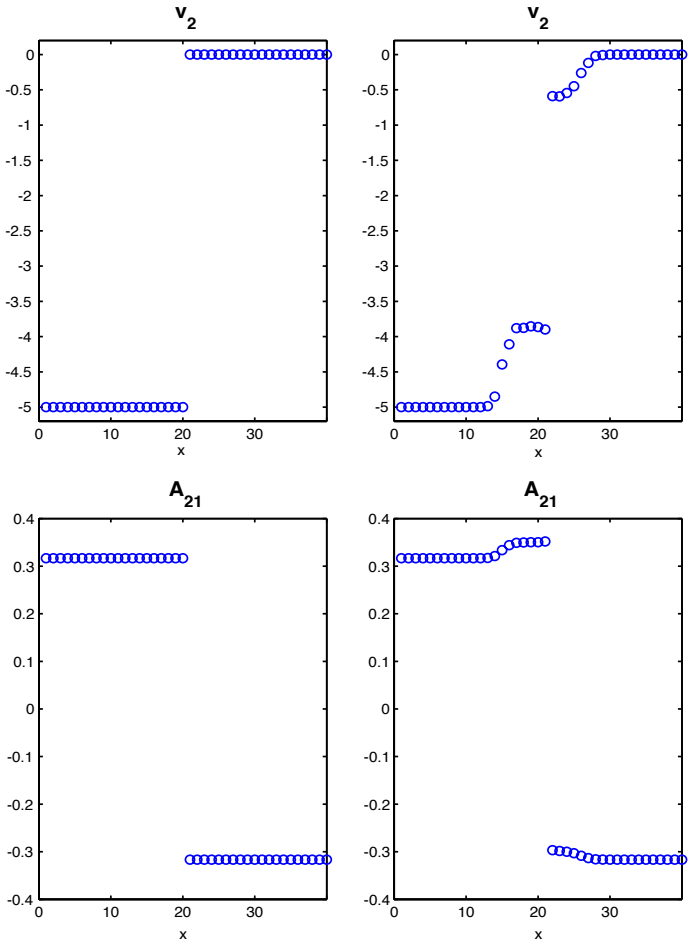

Fig. 19. Left: the initial data for $A_{2,1}$ and v_2 (100 m/s); right: the numerical results in 15 macro-time-steps.

be analogous to the one for thermal gradient effects. We should also be able to replace the molecular dynamics by more refined models such as quantum-mechanical models. The additional work needed is not substantially more than those in Carter (2000), Abraham et al. (1998) and Broughton et al. (1999).

Many aspects of real materials are neglected in the present paper. These include: defect nucleation, defect–defect interaction, and complex defect structures. While in principle they can be handled by the method developed in this paper, there are many practical issues that need to be addressed. As an example, let us discuss defect nucleation. The adaptive model refinement methodology should be able to handle defect nucleation. Once a macroscale cell is identified for potential defect nucleation, the model is locally refined to level of MD, and defect nucleation can be accommodated. Once the defect is sufficiently mature, it can be translated to a

continuum representation. There are at least two obstacles that need to be overcome. One is the criterion for identifying potential defect nucleation sites. This can be defect-dependent. The other is the translation of the defect from atomistic to continuum representation. These issues are common to all multiscale methods, not just HMM. They need to be resolved before multiscale methods become truly useful.

Acknowledgements

We are grateful to Li-Tien Cheng, Bjorn Engquist, Zhongyi Huang, Pingbing Ming, Weiqing Ren and Richard Tsai for very interesting discussions. The work reported here is supported in part by an ONR grant N00014-01-0674 and the National Science Foundation of China through a Class B award for distinguished young scholars 10128102.

Appendix. More general interatomic potentials

We have provided the microscopic definition of the stress and heat flux for pair potentials such as hard sphere, Lennard–Jones and Morse potential. The HMM procedure can be generalized to other potentials. The only different part is the expression for the stress tensor and energy flux, which is provided here for potentials that contains three body interactions, EAM potentials and on site potentials.

Three body interaction: this includes Stillinger–Webber and Tersoff potentials. For three body interaction, we write the energy as

$$V_3(\mathbf{x}_i, \mathbf{x}_j, \mathbf{x}_k) = V(|\mathbf{x}_i - \mathbf{x}_j|, |\mathbf{x}_j - \mathbf{x}_k|, |\mathbf{x}_k - \mathbf{x}_i|).$$

The force exerted on the ith atom is written as

$$\sum_{j,k \neq i} \mathbf{f}_{ijk}$$

with summation over distinct indices j and k. After some tedious calculation, one can verify that $\mathbf{f}_{ijk}$ can be decomposed into two parts: $f_{ijk} = f^{(1)}_{ijk} + f^{(2)}_{ijk}$ with the property that $f^{(1)}_{ijk} = f^{(1)}_{jik}$ and $f^{(2)}_{ijk} = f^{(2)}_{kji}$. Then the stress and energy flux are

$$\begin{aligned}
\widetilde{\boldsymbol{\sigma}}(\mathbf{x}^0, t) = & \frac{1}{2} \sum_{i,j,k} \mathbf{f}^{(1)}_{ijk} \otimes (\mathbf{x}^0_i - \mathbf{x}^0_j) \\
& \times \int_0^1 \delta(\mathbf{x}^0 - (\mathbf{x}^0_j + \lambda(\mathbf{x}^0_i - \mathbf{x}^0_j))) \, \mathrm{d}\lambda \\
& + \frac{1}{2} \sum_{i,j,k} \mathbf{f}^{(2)}_{ijk} \otimes (\mathbf{x}^0_i - \mathbf{x}^0_k) \\
& \times \int_0^1 \delta(\mathbf{x}^0 - (\mathbf{x}^0_k + \lambda(\mathbf{x}^0_i - \mathbf{x}^0_k))) \, \mathrm{d}\lambda
\end{aligned} \tag{25}$$

and

$$\begin{aligned}\widetilde{\mathbf{j}}(\mathbf{x}^0,t) = &\frac{1}{4}\sum_{i,j,k}(\mathbf{v}_i+\mathbf{v}_j)\cdot\mathbf{f}_{ijk}^{(1)}(\mathbf{x}_i^0-\mathbf{x}_j^0)\\ &\times\int_0^1\delta(\mathbf{x}^0-(\mathbf{x}_j^0+\lambda(\mathbf{x}_i^0-\mathbf{x}_j^0)))\,\mathrm{d}\lambda\\ &+\frac{1}{4}\sum_{i,j,k}(\mathbf{v}_i+\mathbf{v}_k)\cdot\mathbf{f}_{ijk}^{(2)}(\mathbf{x}_i^0-\mathbf{x}_k^0)\\ &\times\int_0^1\delta(\mathbf{x}^0-(\mathbf{x}_k^0+\lambda(\mathbf{x}_i^0-\mathbf{x}_k^0)))\,\mathrm{d}\lambda. \end{aligned}\tag{26}$$

EAM potentials: EAM (Embedded-atom method) has recently become the most popular candidate of interatomic potentials for metals. It includes a pair potential and an EAM energy that depends on local electron density,

$$E=\frac{1}{2}\sum_i\sum_j\phi(r_{ij})+\sum_i F_{t_i}(\bar{\rho}_i),\quad \bar{\rho}_i=\sum_{j\neq i}\rho_{t_j}(r_{ij}).$$

Here t_i indicates the atom type and $\mathbf{r}_{ij}=\mathbf{x}_i-\mathbf{x}_j$ with r_{ij} being the magnitude.

Then the stress and the heat flux are expressed as

$$\begin{aligned}\boldsymbol{\sigma}=&-\sum_i\sum_{j>i}(\phi'_{t_it_j}(r_{ij})+F'_{t_i}(\bar{\rho}_i)\rho'_{t_j}(r_{ij})+F'_{t_j}(\bar{\rho}_j)\rho'_{t_i}(r_{ij}))\frac{\mathbf{r}_{ij}\otimes\mathbf{r}_{ij}^0}{r_{ij}}\\ &\times\int_0^1\delta(\mathbf{x}^0-(\mathbf{x}_j^0+\lambda(\mathbf{x}_i^0-\mathbf{x}_j^0)))\,\mathrm{d}\lambda\end{aligned}$$

and

$$\begin{aligned}\mathbf{j}=&\frac{1}{4}\sum_i\sum_{j\neq i}(\mathbf{v}_i+\mathbf{v}_j)(\phi'_{t_it_j}(r_{ij})+F'_{t_i}(\bar{\rho}_i)\rho'_{t_j}(r_{ij})+F'_{t_j}(\bar{\rho}_j)\rho'_{t_i}(r_{ij}))\frac{\mathbf{r}_{ij}\otimes\mathbf{r}_{ij}^0}{r_{ij}}\\ &\times\int_0^1\delta(\mathbf{x}^0-(\mathbf{x}_j^0+\lambda(\mathbf{x}_i^0-\mathbf{x}_j^0)))\,\mathrm{d}\lambda.\end{aligned}$$

External potential: some problems involve an external potential that contains an on-site term: $V_1(\mathbf{x}_i)$. In this case, source terms in the form of

$$\sum_i\mathbf{f}_i\delta(\mathbf{x}^0-\mathbf{x}_i^0)\quad\text{and}\quad-\sum_i\mathbf{f}_i\cdot\mathbf{v}_i\delta(\mathbf{x}^0-\mathbf{x}_i^0),$$

should be added to the right-hand side of the second and third conservation laws in Eq. (9), respectively.

References

Abeyaratne, R., Knowles, J.K., 1991. Kinetic relation and the propagation of phase boundaries in solids. Arch. Ration. Mech. Anal. 114, 119–154.

Abeyaratne, R., Bhattacharya, K., Knowles, J.K., 2000. Strain-energy functions with multiple local minima: modeling phase transformations using finite thermoelasticity. Nonlinear Elasticity, Theory and Application. Cambridge University Press, Cambridge.

Abraham, F.F., Broughton, J.Q., Bernstein, N., Kaxiras, E., 1998. Spanning the coninuum to quantum length scales in a dynamic simulation of brittle fracture. Europhys. Lett. 44 (6), 783–787.

Arroyo, M., Belytschko, T., 2000. Finite element for the nonlinear mechanics of crystalline sheets and nanotubes. Int. J. Numer. Methods Eng. 00, 1–6.

Ball, J.M., James, R.D., 1987. Fine phase mixtures as minimizers of energy. Arch. Ration. Mech. Anal. 100, 13–52.

Ball, J.M., James, R.D., 1992. Proposed experimental tests of a theory of fine microstructure and the two-well problem. Phil. Trans. Roy. Soc. London A 338, 389–450.

Becquart, C.S., Clapp, P.C., Rifkin, J.A., 1993. Molecular-dynamics simulations of tweed structure and the ω phase in Ni–Al. Phys. Rev. B 48, 6–13.

Bhattacharya, K., 2003. Microstructure of Martensite. Why it Forms and How it Gives Rise to the Shape-memory Effect. Oxford University Press, Oxford.

Brandt, A., 2002. Multiscale scientific computation: Review 2001. In: Barth, T.J. et al. (Eds.), Lecture Notes in Computational Science and Engineering. Springer, Berlin.

Broughton, J.Q., Abraham, F.F., Bernstein, N., Kaxiras, E., 1999. Concurrent coupling of length scales: methodology and application. Phys. Rev. B 60, 2391–2402.

Cai, W., de Koning, M., Bulatov, V.V., Yip, S., 2000. Minimizing boundary reflections in coupled-domain simulations. Phys. Rev. Lett. 85, 3213.

Cancès, E., Castella, F., Chartier, Ph., Faou, E., Le Bris, C., Legoll, F., Turinici, G., 2004. High-order averaging schemes with error bounds for thermodynamical properties calculations by MD simulations, INRIA research report RR-4875. J. Chem. Phys., accepted for publication.

Car, R., Parrinello, M., 1985. Unified approach for molecular dynamics and density-functional theory. Phys. Rev. Lett. 55, 2471–2474.

Carter, E.A., 2000. Orbital-free density functional theory dynamics: evolution of thousands of atoms with quantum forces. In: Atluri, S.N., Brust, F.W., (Eds.), Advances in Compuational Engineering and Sciences, 1967. Tech Science Press, Palmdale.

Chakravorty, S., Wayman, C.M., 1976. Thermoelastic martensitic-transformation in beta' Ni–Al alloys. Metall. Trans. A 7 (4), 555–582.

Cormier, J., Rickman, J.M., Delph, T.J., 2001. Stress calculation in atomistic simulations of perfect and imperfect solids. J. Appl. Phys. 89, 99–104.

E, W., Engquist, B., 2002. The heterogeneous multi-scale methods. Commun. Math. Sci. 1 (1), 87–132.

E, W., Engquist, B., Li, X., Ren, W., Vanden-Eijnden, E., The heterogeneous multiscale method: a review, SIAM Rev., submitted for publication.

E, W., Huang, Z., 2001. Matching conditions in atomistic-continuum modeling of material. Phys. Rev. Lett. 87, 135501.

E, W., Huang, Z., 2002. A dynamic atomistic-continuum method for the simulation of crystalline material. J. Comput. Phys. 182, 234–261.

Engquist, B., Tsai, Y.H., The heterogeneous multiscale methods for a class of Stiff ODEs. Math. Comput., in press.

E, W., Li, X., 2004. Analysis of the heterogeneous multiscale method for gas dynamics. Methods Anal. Appl., submitted for publication.

E, W., Li, X., 2005. Multiscale modeling of crystalline solids. Handbook of Computational Material Science, to appear.

E, W., Li, X., Vanden-Eijnden, E., 2004. Some recent progress in multiscale modeling. In: Attinger, S., Koumoutsakos, P., (Eds.), Multiscale Modeling and Simulation, Lecture Notes in Computational Science and Engineering, vol. 39. Springer, Berlin.

Ercolessi, F., Adams, J.B., 1994. Interatomic potentials from first-principles calculations: the force-matching method. Europhys. Lett. 26, 583.

Frenkel, D., Smit, B., 2002. Understanding Molecular Simulation: From Algorithms to Applications. Academic Press, New York.

FronTier, the software for front track method, http://galaxy.ams.sunysb.edu/FTdownload/.

Garcia, A.L., Bell, J.B., Crutchfield, W.Y., Alder, B.J., 1999. Adaptive mesh and algorithm refinement using direct simulation Monte Carlo. J. Comput. Phys. 154, 134–155.

Glimm, J., Li, X.L., Liu, Y., 2002. Conservative front tracking in one space dimension, fluid flow and transport in porous media: mathematical and numerical treatment (South Hadley, MA, 2001). Contemp. Math. 295, 253–264.

Glimm, J., Li, X.L., Shyue, K.M., Zhang, Q., Zheng, Y., 1998. Three dimensional front tracking. SIAM J. Sci. Comput. 19, 703–727.

Godlewski, E., Raviart, P.A., 1996. Numerical Approximation of Hyperbolic Systems of Conservation Laws. Springer, New York.

Irving, J.H., Kirkwood, J.G., 1950. The statistical mechanical theory of transport processes IV. J. Chem. Phys. 18, 817–829.

Knap, J., Ortiz, M., 2001. An analysis of the Quasicontinuum method. J. Mech. Phys. Solid 49, 1899.

Landau, L.D., 1986. Theory of Elasticity. Elsevier Science Ltd., Amsterdam.

LeVeque, R., 1992. Numerical Methods for Conservation Laws. Birkhäuser, Bosel.

Li, Z.P., 2001. Computations of needle-like microstructures. Appl. Numer. Math. 39, 1–15.

Lu, G., Kaxiras, E., 2005. An overview of multiscale simulations of materials. In: Rieth, M., Schommers, W. (Eds.), Handbook of Theoretical and Computational Nanotechnology, in press.

Luskin, M., 1996. On the computation of crystalline microstructure. Acta Numer. 5, 191–258.

Miller, R.E., Tadmor, E.B., 2002. The Quasicontinuum method: overview, applications and current directions. J. Comput.-Aided Mater. Des. 9, 203–239.

Nessyahu, H., Tadmor, E., 1990. Nonoscillatory central differencing for hyperbolic conservation laws. J. Comput. Phys. 87, 408–463.

Nishiyama, Z., 1978. Martensitic Transformation. Academic Press, New York.

Oden, J.T., Vemaganti, K.S., 2000. Estimation of local modeling error and goal-oriented adaptive modeling of heterogeneous materials. I. Error estimates and adaptive algorithms. J. Comput. Phys. 164, 22–47.

Pinsook, U., Ackland, G.J., 2000. Atomistic simulation of shear in a martensitic twinned microstructure. Phys. Rev. B 62, 5427–5434.

Purohit, P.K., Bhattacharya, K., 2003. Dynamics of strings made of phase-transforming materials. J. Mech. Phys. Solids 51, 393–424.

Rudd, R.E., Broughton, J.Q., 1998. Coarse-grained molecular dynamics and the atomic limit of finite element. Phys. Rev. B 58 (10), 5893–5896.

Shenoy, V.B., Miller, R., Tadmor, E.B., et al., 1998. Quasicontinuum models of interfacial structure and deformation. Phys. Rev. Lett. 80 (4), 742–745.

Shenoy, V.B., Miller, R., Tadmor, E.B., Rodney, D., Phillips, R., Ortiz, M., 1999. An adaptive finite element approach to atomic-scale mechanics-the quasicontinuum method. J. Mech. Phys. Solids 47, 611–642.

Slemrod, M., 1983. Admissibility criterion for propagating phase boundaries in a van der Waal fluid. Arch. Ration. Mech. Anal. 81, 301–315.

Tadmor, E.B., Ortiz, M., Phillips, R., 1996. Quasicontinuum analysis of defects in crystals. Philos. Mag. A 73, 1529–1563.

Truskinovsky, L., Vainchtein, A., 2003. Peierls–Nabarro landscape for martensitic phase transitions. Phys. Rev. B 67, 172103.

Voter, A.F., Chen, S.P., 1987. Accurate interatomic potential for Ni, Al, and Ni3Al. Mater. Res. Soc. Proc. 82, 175–180.

Wagner, G.J., Liu, W.K., 2003. Coupling of atomistic and continuum simulations using a bridging scale decomposition. J. Comput. Phys. 190, 249–274.

Wagner, G.J., Eduard, G.K., Liu, W.K., 2004. Molecular dynamics boundary conditions for regular crystal lattice. Comput. Method Appl. Mech. Eng. 193, 1579–1601.

Yang, J., 2006. Ph.D. Thesis, Princeton University.

Zhou, M., 2003. A new look at the atomic level virial stress: on continuum-molecular system equivalence. Proc. Roy. Soc. London A 459, 2347–2392.

Zimmerman, J.A., Webb III, E.B., Hoyt, J.J., Jones, R.E., Klein, P.A., Bammann, D.J., 2004. Calculation of stress in atomistic simulation. Modelling Simul. Mater. Sci. Eng. 12, S319–S332.